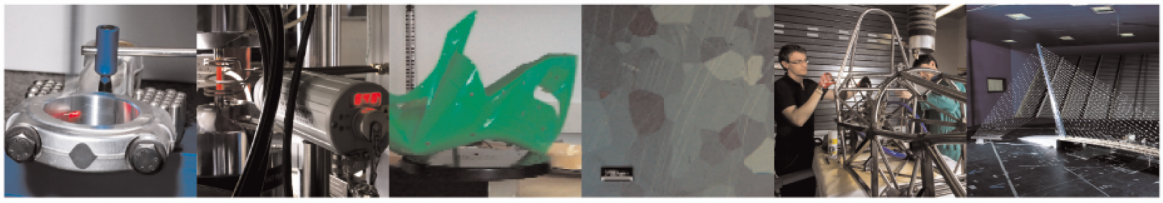

A hybrid numerical-analytical-experimental framework to estimate the surface state and fatigue performance of laser powder bed fusion materials after surface treatment of shot peening

Khajehmirza H.;Heydari Astaraee A.;Monti S.;Guagliano M.;Bagherifard S.

This is a post-peer-review, pre-copyedit version of an article published in Applied Surface Science. The final authenticated version is available online at: https://doi.org/10.1016/j.apsusc.2021.150758

DIPARTIMENTO DI MECCANICA ■ POLITECNICO DI MILANO
via G. La Masa, 1 ■ 20156 Milano ■ EMAIL (PEC): pecmecc@cert.polimi.it
http://www.mecc.polimi.it
Rev. 0

A hybrid numerical-analytical-experimental framework to estimate the surface state and fatigue performance of laser powder bed fusion materials after surface treatment of shot peening

Hamed Khajehmirza, Asghar Heydari Astaraee, Stefano Monti, Mario Guagliano, Sara Bagherifard
Politecnico di Milano, Department of Mechanical Engineering, Milan, Italy

Abstract

Despite the rapid growth of additive manufacturing (AM) technologies, AM parts usually present relatively poor surface quality in as-built condition. This necessitates the application of customized post surface treatments to efficiently enhance the surface quality and alleviate the adverse effects of high surface roughness and extremely irregular surface morphology on fatigue strength of AM metallic materials. In this paper, starting from an as-built AM surface, a detailed numerical model is developed to effectively estimate the surface morphology of laser powder bed fusion (LPBF) AlSi10Mg specimens after shot peening, in terms of standard roughness parameters. The obtained results are then incorporated into two analytical approaches to evaluate the fatigue strength of different series. The accuracy of the model is validated by comparisons made with experimental data obtained considering as-built and shot peened specimens both before and after heat treatment. The results demonstrate that the proposed hybrid approach can serve as a powerful package not only to determine the beneficial contribution of shot peening on the surface morphology of rough AM material but also to provide an accurate and rather reliable approximation of their fatigue strength.

Keywords: Shot peening, AlSi10Mg, Additive manufacturing, Surface roughness, Fatigue performance

Nomenclature

S_a	Areal arithmetic average height
S_q	Areal root mean square deviation
S_z	Areal maximum valley to peak height
S_{10z}	Areal 10-points height
S_p	Areal maximum height of peaks
S_v	Areal maximum depth of valleys
R_a	Arithmetic average height
d	Average grain size
$\overline{K}_f$	Equivalent fatigue notch factor
$\overline{K}_t$	Equivalent stress concentration factor
K_D	Exponent constant
A, B, n	Material model constants
R_t	Maximum valley to peak height
R_p	Maximum peak height
R_v	Maximum valley depth
q	Notch sensitivity
R_q	Root mean square deviation
b	Fatigue test specimen diameter
m	Stress state constant
R_z	Ten-points height
μ	Coulomb friction coefficient
λ_{xc}, λ_{yc}	Cut-off wavelengths
$\bar{\rho}$	Effective notch radius
σ_{bf}	Fatigue strength in bending
σ_{tf}	Fatigue strength in tension
σ_f	Fatigue strength in local stress method
$\acute{\sigma}_e$	Fatigue strength of notched specimen
σ_e	Fatigue strength of unnotched specimen
σ	Flow stress
α	Gaussian constant

σ_{max}	Maximum local stress
ε	Plastic strain
$\acute{\chi}$	Relative stress gradient
χ	Stress gradient
AM	Additive manufacturing
AB	As-built specimen
PEEQ	Equivalent plastic strain
FE	Finite element
HT+SP	Heat-treated shot peened specimen
HT	Heat-treated specimen
LPBF	Laser powder bed fusion
SLM	Selective laser melting
SP	Shot peening
UTS	Ultimate tensile strength

1. Introduction

One of the most prominent elements causing a barrier for the advancement of additive manufacturing (AM) is the cost of the whole cycle, from powder feedstock to post-processing [1, 2]. According to a recent research, a substantial portion (up to 40%) of the overall cost of AM is not due to the printing process itself, but to the necessity of pre and post-manufacturing processes [3]. This is emphasized by the growing attention dedicated to the definition of often customized post-treatment methods for AM components. Despite the rather promising capabilities of the fast-growing AM technologies in fabricating components with intricate geometrical characteristics, a common limiting issue is the low surface quality obtained in the as-built condition. The surface defects and irregularities are caused by a variety of factors including partially melted powders (for powder-bed processes), balling effects, spatters, inadequate fusion, stair-case effect, and imprecise support removal. The uncontrolled surface roughness can significantly deteriorate a series of performance indexes including fatigue strength, wear and corrosion resistance, besides interfering with geometrical accuracy, and aesthetical features. Hence, imposing a considerable barrier against prospective applications of AM.

Different experimental studies have reported the adverse effects of high surface roughness on the cyclic behavior of as-built laser powder bed fusion (LPBF) specimens considering their notably inferior fatigue strength compared to conventionally manufactured counterparts. Mower et al. [4] demonstrated that rotating bending fatigue strength of LPBF AlSi10Mg specimens was 60% of that of the wrought material. This reduction was attributed to the much higher surface roughness and the numerous stress-concentrating defects in the AM specimens compared to the wrought material. Beretta et al. [5] reported the three-point bending fatigue strengths of as-built LPBF AlSi10Mg specimens to be in the range of 50-75% of that of the machined series, highlighting again the significant contribution of surface roughness to fatigue strength reduction.

To consider the significant role of surface roughness on fatigue strength, recently few studies have focused on developing also numerical or analytical methods to bring the surface roughness into fatigue life estimations for AM materials. Vayssette et al. [6] estimated the effect of surface roughness on high cycle fatigue behavior of LPBF Ti6Al4V specimens using a numerical approach based on extreme values statistics of a non-local fatigue indicator parameter. They reported a drastic drop of 60% in the fatigue strength of as-built specimen due to the poor surface roughness with respect to hot-rolled series. Sanaei and Fatemi [7] assessed the effects of the intrinsic surface roughness in AM on fatigue performance of LPBF Ti6Al4V confirming the strong effect of surface roughness, that overshadowed the specimen's microstructure. Chen et al. [8] claimed that the most dominant factor in limiting fatigue performance of as-built LPBF Ti6Al4V is the poor surface quality by making a comparison of fatigue strengths before and after surface machining. Pegues et al. [9] investigated the impact of surface roughness on the fatigue strength of LPBF Ti6Al4V specimens by defining a stress concentration factor. Roughness parameters of a linear profile along specimen's longitudinal direction were implemented to obtain an equivalent stress concentration factor using the well-established analytical method proposed by Arola and Ramulu [10]. Despite providing significant insight on the contribution of surface roughness in fatigue strength of AM materials, the majority of the numerical or analytical studies rely

solely on the extraction of linear roughness parameters of a few profiles from the specimen's surfaces, rather than more representative areal roughness parameters.
Considering the importance of this topic, the implementation of multiple cost-efficient post treatments has recently attracted more attention to improve the surface quality and therefore, the fatigue performance of AM specimens and components [11]. Mechanical surface treatments, in particular shot peening, have proved to be successful in significantly enhancing the fatigue strength of as-built AM specimens. Shot peening is a cold working surface treatment in which a stream of metallic, glass or ceramic shots, bombard the surface of the target material under controlled intensity and coverage to induce surface plastic deformation [12]. In a recent experimental study, we showed that shot peening with controlled parameters can induce a smoother and more regular surface morphology leading to considerably enhanced fatigue strength in LPBF AlSi10Mg specimens [13]. The effect of shot peening in removing surface irregularities and improving the surface roughness of the LPBF AlSi10Mg specimens was confirmed also by Maamoun et al. [14]. Few other studies have established the considerable fatigue strength improvement of additive manufactured Ti6Al4V specimens after shot peening [15-19].
The objective of this study is to provide a framework to account for the effect of shot peening and its contribution to roughness modulation and fatigue strength enhancement in AM material. To this aim, first, a robust numerical model capable of simulating multiple impact shot peening process on the highly irregular surface of as-built AM material was developed. A detailed MATLAB code was prepared to extract an inclusive list of profile and areal surface roughness parameters from the simulation output. Comparison with experimental data confirmed that the model can deliver an accurate prediction of roughness parameters before and after shot peening process. Then, two analytical approaches were implemented to relate the calculated areal roughness parameters to the fatigue strength of the specimens. Comparison with experimental fatigue strength data (reported in the author's previous study [13]), confirmed the validity of the developed numerical-analytical approach to provide an accurate fatigue strength estimation after shot peening. The presented hybrid approach can successfully assess the effect of shot peening on homogenization of the as-built surfaces and can evaluate their contribution to fatigue strength enhancement. This package can be significantly practical for shot peening parameter optimization in AM sector, as it can substantially reduce if not eliminate the needed costly trial and error phase on experimental tuning of shot peening parameters and the following fatigue tests.

2. Materials and methods

2.1. Specimens

The specimens were manufactured by means of LPBF technology using gas atomized AlSi10Mg powder (SLM solutions group AG, DE) with the nominal chemical composition presented in **Error! Reference source not found.** and an average particle diameter of 50 μm. The specimens were fabricated using an SLM 500HL machine with a build chamber of 280×500×350 mm^3 equipped with four Yttrium fiber lasers working simultaneously. The process parameters were selected as follows: laser power of 350 W, spot diameter of 78 μm, scan speed of 1150 mm/s, hatch distance of 0.17 mm, layer thickness of 50 μm, and a density equal to 35.81 [J/mm^3]. The manufacturing direction was vertical based on a scanning strategy of 67° rotation between successive layers. Re-melting occurred each time in the contour zone prior to the subsequent layer deposition. Dog bone specimens following ISO 6892-1 standard as shown in Figure 1a were used for the study. The surface on which surface roughness measurements were performed were the flat part of the specimens parallel to the vertical build direction. The surface topography of the specimens in the as-built condition is shown in Figure 1b, taken by a Zeiss EVO50 scanning electron microscope (SEM).

Table 1 Nominal chemical composition of AlSi10Mg powder provided by the supplier

Element (wt%)	Al	Si	Fe	Cu	Mn	Mg	Zn	Ti

Minimum	Balance	9.0	-	-	-	0.2	-	-
Actual	Balance	9.8	0.24	<0.005	<0.005	0.44	<0.002	<0.01
Maximum	Balance	11	0.55	0.05	0.45	0.45	0.1	0.15

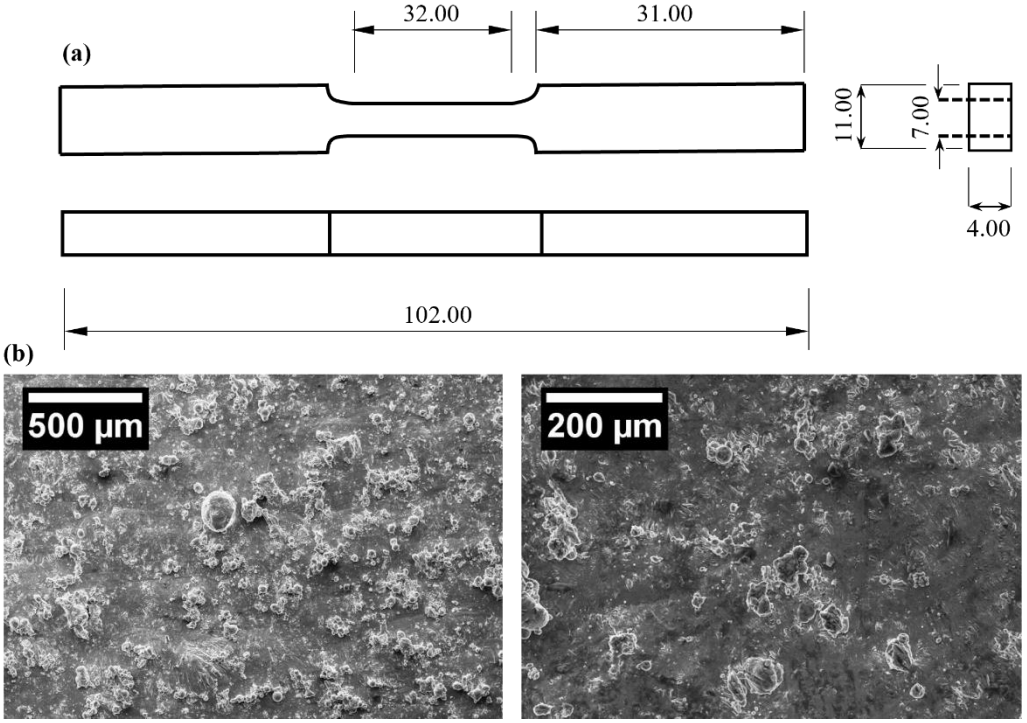

Figure 1. a) Geometry of dog bone specimens used for tensile tests b) top view SEM micrographs of AB specimens at different enlargements.

A number of specimens underwent T6 thermal treatment, which was performed following the interval times and temperature range suggested in [20]. The T6 heat-treatment was performed firstly heating the specimen up to 520 ℃, followed by a solution heat treatment for 1 h, quenching in water (-160 ℃/min) for 1 h, and finally heating up to 160 ℃ and aging for 6 h at this temperature. The heat treatment was concluded by a final quenching step in water following the work of Gharavi et al. [21]. The as-built and heat-treated specimens were later subjected to shot peening using steel shot 170H medium with a nominal diameter of 0.43 mm at an Almen Intensity of 10 A (0.001 inch) until reaching a full surface coverage. Four different series of as-built (AB), heat-treated (HT), shot peened (SP), and heat treated and shot peened (HT+SP) were considered in this study.

2.2. Experimental surface roughness measurements

Surface roughness of all series was evaluated using an Alicona Infinite Focus optical 3D measurement system utilizing the surface texture measurement module. Two sets of standard roughness parameters, namely linear and areal, were included. To enable a valid comparison of the experimental data with the numerical results, which were based on a 1×1 mm^2 scanned surface area (discussed later in model description), at least 7 areas of 1×1 mm^2 were scanned on random surface locations for each series. The areal roughness parameters were calculated after applying a 3D Gaussian filter using a cut-off wavelength of 0.25 mm following ISO 4288:1996. A custom-made MATLAB code was developed to extract the areal roughness parameters from the output of numerical simulations. The code was implemented also on the experimentally scanned STL files, the results of which were compared with the parameters directly provided by Alicona Infinite Focus microscope to validate the code.

2.3. Finite element (FE) simulations

2.3.1. FE model geometry

To numerically simulate the single, as well as multiple-impact shot peening on AB and HT AlSi10Mg specimens, a three-dimensional (3D) model was developed using the commercial FE software

Abaqus/Explicit 2019. The proposed impact area for the simulation was 1×1 mm^2 in size to reduce computational costs, considering the experimental shot size and velocity. Three representative surface areas of 1.2×1.2 mm^2, randomly taken from the experimental AB specimen surface, were used in the modeling to serve as representative impact areas. The modeling and simulation were repeated for these three surfaces in order to check the data variability. The experimental surface topography data obtained from the Alicona microscope were directly imported into the FE software through an STL file. The three characteristic surfaces were slightly modified to relieve the extremely sharp peaks and valleys and tiny irregular deformities of the surface, as depicted in Figure 2. This filtering was implemented by transformation of the mesh element faces into a geometry considering a sufficient stitching tolerance to guarantee a smoothly connected generated surface. This step was essential to create a 3D model that could be meshed successfully to perform the simulations at an affordable computational cost. The larger surface with respect to the target impact area (1×1 mm^2) was to ensure that the shots impacting the regions near the boundaries of the impact area were experiencing the same surface conditions as the inside surface. Since the heat treatment does not affect the surface features, the same representative surfaces were used for both AB and HT cases. The effect of this surface transformation on the accuracy of the obtained results was evaluated as described in the next sections.

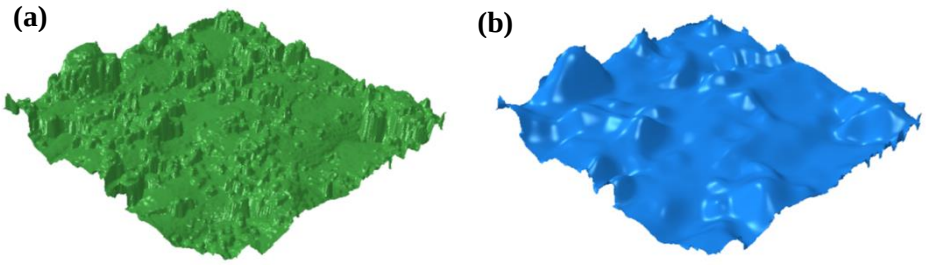

Figure 2. The process of transforming the highly irregular and rough as-built surfaces: a) original orphan mesh with removed elements for better representation b) transformed surface obtained by a transformation from mesh element faces into a geometry

The size of the whole part for numerical simulation was considered sufficiently large, as shown in Figure 3a, to avoid the effect of boundary conditions on the deformation state in the impact area. The irregular initial surface was positioned at the center of the upper part and was completely confined by the surrounding flat areas. The impact area and the adjacent connecting surfaces were meshed using C3D4 (4-node linear tetrahedron) elements with a minimum mesh size of 18 μm, being approximately $1/12^{th}$ of dimple diameter. The dimple area was estimated as the diameter of an indent formed by an individual shot impact on a flat surface. The rest of the target body away from the impact surface was meshed with C38DR elements (8-node linear brick with reduced integration and hourglass control). The side and bottom faces of the target body were surrounded by half-infinite CIN3D8 elements (8-node linear), which provided quiet boundaries by minimizing the reflection of dilatational and shear waves back into the area of interest [22]. Infinite elements take into account only linear elastic behavior; therefore, they must be positioned reasonably distant from the non-linear interaction region to ensure the accuracy of the simulation. The steel shot was considered as a spherical deformable body with a diameter of 0.43 mm, similar to the experimental average shot size, and was meshed using a C3D4 (4-node linear tetrahedron) element type with an element size of 21 μm.

A general contact with tangential behavior and Coulomb friction coefficient equal to 0.2 [23] was assigned for the whole model. Moreover, an average impact velocity of 65 m/s regarding the Almen intensity and shot size used in the experiments was estimated following the empirical method suggested in [24] as an initial condition for all shots with an impact angle of 90°.

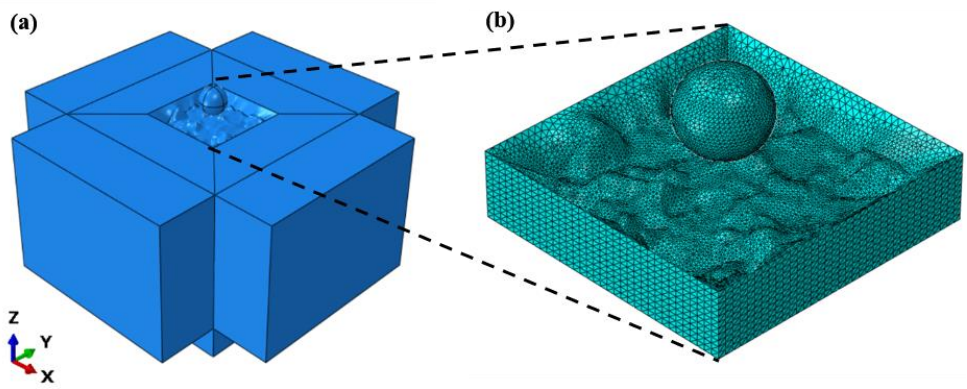

Figure 3. a) Geometry of the model including the main target volume, b) mesh details of the impact region as well as the shot

2.3.2. Material model

A set of experimental tensile tests were performed on AB and HT specimens following ISO 6892-1 instructions using an MTS Alliance machine at a strain rate of 0.7 mm/min up to 2% strain followed by a constant rate of 2 mm/min. Three specimens were tested for each series in order to find the average behavior. The tensile properties are reported in Table 2 and the resultant mean stress-strain curves of the specimens are provided in Figure 4.

Table 2 Monotonic mechanical properties of LPBF AlSi10Mg specimens

	As-built (AB)	Heat-treated (HT)
Young's modulus (GPa)	73 ± 1.5	74 ± 1.5
Yield stress (MPa)	274 ± 2	199 ± 8
Ultimate tensile strength (MPa)	394 ± 16	264 ± 12
Elongation at failure (%)	2.4 ± 0.3	13 ± 0.9

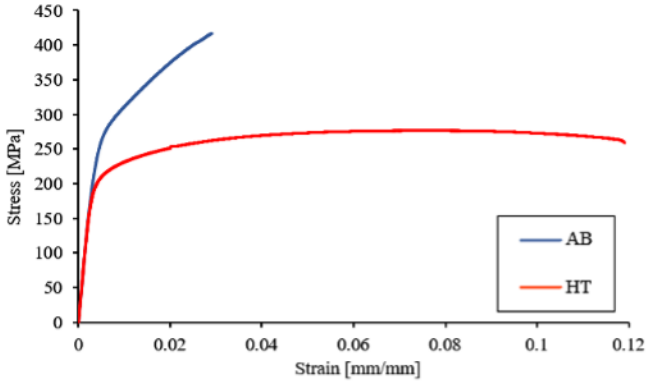

Figure 4. The engineering stress-strain curve of AB and HT specimens

Since shot peening is a process that leads to large plastic deformations on the surface, it is necessary to implement a constitutive material model that can consider the plastic behavior of the AlSi10Mg target material in the simulations. Thus, the experimental stress-strain curves were fitted using Ludwik's law (Eq. 1) [25]:

$$\sigma = A + B.\varepsilon^{n} \qquad \text{Eq. 1}$$

where σ is the flow stress, ε is the plastic strain, and A, B and n are material model constants. The fitting is beneficial to extrapolate the flow behavior of the material at large plastic strains caused by shot peening. Parameter A represents the elastic limit in the stress-strain curve obtained from the experimental tensile tests (Figure 4). By fitting the experimental data of true stress versus true plastic

strain using Eq. 1, coefficient *B* and *n* constant were estimated. The final sets of estimated parameters for the material model of AB and HT series are presented in Table 3.

Table 3. Ludwik material model parameters estimated for AlSi10Mg

Specimen	A (MPa)	B (MPa)	n
AB	150.3	1144	0.3761
HT	117	313	0.1968

2.3.3. Coverage estimation

To correctly capture the intrinsic randomness of the shot peening process, the developed FE model shall include a certain number of shots bombarding the target areas at random locations. Surface coverage is defined as the ratio of the area covered by plastic indentation to the total area of the target surface demonstrated in percentages [26]. The straightforward method for coverage estimation on flat surfaces and, thus calculation of the required number of shots, is usually based on the displacement field, i.e., an individual indent size of a single impact [27]. Some researchers utilized the well-known Avrami model to estimate the shot numbers to achieve full coverage based on the individual indent size of a single impact [28]. However, this method is not applicable in the current study due to the extremely irregular surface of as-built AM specimens; this high surface irregularity in the not peened state leads to the inhomogeneity of the indent size based on the impact location. Thus, the coverage was alternatively estimated based on the strain field. Miao et al. [29] suggested a method using the distribution of equivalent plastic strain (PEEQ) to evaluate surface coverage in shot peening. In this method, surface coverage is described by the ratio of the number of nodes with a PEEQ larger than a certain threshold value over the total number of nodes on the impact area. To estimate the threshold value, a single impact model was created considering a completely flat impact area. All the other parameters including the element size of the impact area and material properties were maintained.

A MATLAB code was developed to generate a random impact sequence and arrangement for the multiple shots. A random function was implemented to generate the set of coordinates in *x* and *y* directions inside the impact area. Each shot was positioned at the height corresponding to the outer flat surface surrounding the impact area. This was to ensure that all shots, irrespective of their random positions, were placed higher than the maximum peak present within the impact area. A Python script was implemented to handle the multiple impact shot peening. This was accomplished by creating as many shots as desired, running single-impact analyses one after another with prescribed random positions from the MATLAB code, and sequentially accumulating their effects. Hence, the shot peening simulation was continued until 100% coverage was achieved.

2.4. Numerical surface roughness analysis

2.4.1. Development of the roughness code

A MATLAB subroutine was developed to calculate the standard surface roughness parameters from the output of multiple impact shot peening simulation. The code was validated through comparison with experimental surface roughness data. Using the displacement field obtained for the shot peened representative surfaces (three surfaces per AB, SP and HT+SP series, each) as input, this code firstly removed the slope of the surface mean plane in the *Z* (vertical) direction to bring the surface to the *xy*-plane; then, it determined the position of the mean plane of the surface to serve as a height reference. Afterward, a low-pass 3D Gaussian filter was applied to the surface, as described in Eq.2:

$$S(x,y) = \frac{1}{\alpha^2.\lambda_{xc}.\lambda_{yc}} \exp\left[-\left[\pi\left(\frac{x}{\alpha.\lambda_{xc}}\right)^2 + \pi\left(\frac{y}{\alpha.\lambda_{yc}}\right)^2\right]\right] \quad \text{Eq. 2}$$

where S(x,y) represents the weighting function of the 3D Gaussian filter, λ_{xc} and λ_{yc} are the long cut-off wavelengths in x and y directions, sequentially and $\alpha = \sqrt{ln2/\pi} = 0.4697$. This filtering approach as suggested by ISO 16610-61:2015 is aimed at separating the low frequency features (waviness) from higher frequency ones (roughness). Finally, a set of standard linear and areal roughness parameters were

calculated for each of AB, SP, and HT+SP series following ISO 4287:1997 and ISO 25178 [30]. The profile parameters include R_a (arithmetic average height), R_t (maximum valley to peak height), R_p (maximum height of peaks), R_v (maximum depth of valleys), R_z (ten-points height) and R_q (root mean square deviation), whereas the areal parameters are S_a (arithmetic average height), S_q (root mean square deviation), S_z (maximum valley to peak height) and S_{10z} (ten-points height).

2.5. Estimation of fatigue strength

Two analytical fatigue assessment approaches were implemented to relate the surface state of the shot peened specimens to their fatigue performance. The estimations were then compared with the experimental fatigue strength data associated with three million cycles calculated following the statistical approach suggested in ISO12107 in a previous study of the authors [13]. The experimental data correspond to room temperature rotating bending fatigue tests (stress ratio (R) = -1) performed following the stair-case method [31] with the step size of 10 MPa. Fatigue tests have been carried out on hourglass specimens made with the same material and geometry (Figure 5a) and the same fabrication and shot peening parameters used in the analytical and numerical approaches in this study. The implemented analytical approaches are described below.

2.5.1. Method 1- Equivalent notch factor

Arola and Ramulu [10] proposed an analytical approach to relate surface roughness of an arbitrary surface texture to fatigue life estimations by defining an effective stress concentration factor $\overline{K_t}$ represented as follows:

$$\overline{\mathrm{K}}_{\mathrm{t}} = 1 + \mathrm{m}\left(\frac{\mathrm{R_a}}{\bar{\rho}}\right)\left(\frac{\mathrm{R_t}}{\mathrm{R_z}}\right) \qquad \text{Eq. 3}$$

where $\bar{\rho}$ is the effective notch radius of a roughness profile and the parameter *m* refers to stress state (m=1 for shear and m=2 for tension). $\overline{K_t}$ that is defined for an ideal sinusoidal surface height distribution of constant amplitude and period, considers both shape and depth of the notch. The ratio of R_a over $\bar{\rho}$ represents this sinusoidal waveform in which R_a demonstrates the amplitude and $\bar{\rho}$ is the period. The proposed approach was successfully used in incorporating the effect of surface roughness in fatigue strength of conventionally manufactured polymeric composites and steel materials with different surface textures [10, 32, 33].

To enhance the accuracy of the estimations, in the current study, the whole surface and not only a linear roughness profile is considered for roughness assessment. Thus, we replaced the linear roughness parameters in Eq. 3 with their equivalent areal counterparts and considered $\bar{\rho}$ as the effective valley radius evaluated on the whole target surface (Eq. 4). The areal roughness parameters would potentially provide a more comprehensive contribution of the surface rather than local profile parameters.

$$\overline{\mathrm{K}}_{\mathrm{t}} = 1 + \mathrm{m}\left(\frac{\mathrm{S_a}}{\bar{\rho}}\right)\left(\frac{\mathrm{S_z}}{\mathrm{S_{10z}}}\right) \qquad \text{Eq. 4}$$

Arola and Ramulu [10] considered $\bar{\rho}$ as the apparent notch radius of the prominent profile valleys. Adapting their approach to AM cases, Pegues et al. [9] selected this parameter as the average curvature radii of the five deepest valleys. Herein, however, we implemented a variation for defining the notch radius in each valley; we also considered the prominent valleys for evaluation of the effective notch radius $\bar{\rho}$. To this aim, the three-point peak criterion suggested by Greenwood and Johnson [34] was considered to calculate the asperity radius of a peak in a 2D roughness profile. This definition was applied here only to the valleys, identifying each valley as a point lower than its two adjacent sites (Figure 5b). The radius of each valley (ρ) was then obtained from the radius of the circle passing through the root point and its two neighboring points. An additional condition was implemented following the proposal of Poon and Bhushan [35] stating that the difference in the depths of the two adjacent points of a valley from the valley itself must be higher than a certain threshold value represented as a percentage of R_q parameter of the roughness profile for the valley to be considered for radius

calculation. This threshold value was set specially to consider just the sharpest valleys in the average of the selected radii of each profile.

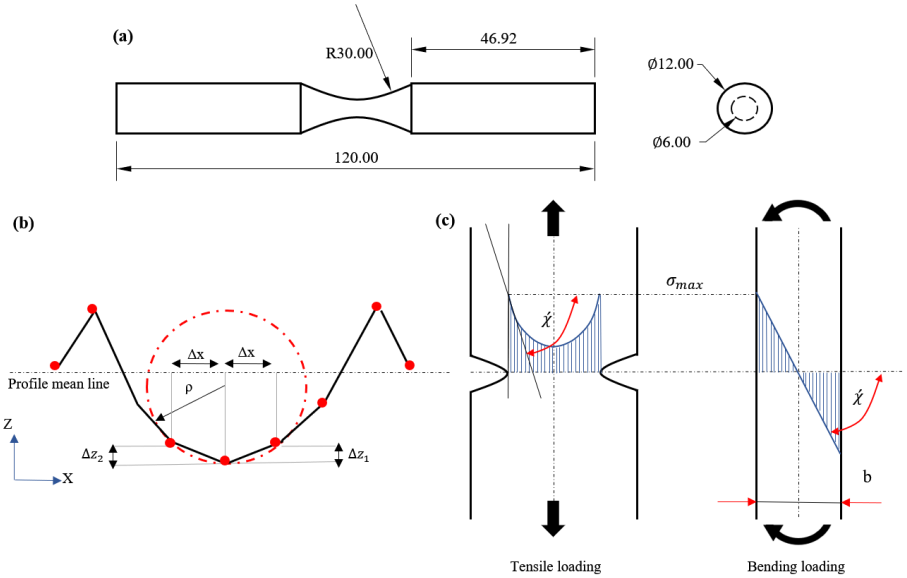

Figure 5. a) schematic geometry of the hourglass specimen used in experimental fatigue tests, b) schematic description of the 3-point method used to calculate valley radii, c) relative stress gradient for tensile loading of a notched specimen and bending of an unnotched specimen

The notch sensitivity factor q was then estimated using Peterson's approach as described in Eq. 5 [36]:

$$q = \left(\frac{1}{1 + \frac{\alpha}{\bar{\rho}}} \right) \quad \text{Eq. 5}$$

where $\bar{\rho}$ represents the equivalent valley radius described above. α is a material characteristic length defined as an index of strength and is commonly considered to be related to grain size [9, 37]. In this study, α is selected as the average grain size of the AB and HT AlSi10Mg specimens assuming that shot peening with a 100% coverage has a very limited effect on grain refinement. The average grain size of the AB specimen was experimentally measured approximately to be 1 µm (Figure S1), and this value was evaluated to be 5 µm for the HT specimens [38]. The equivalent fatigue notch factor $\overline{K_f}$ and fatigue strength $\acute{\sigma}_e$ were calculated using Eq. 6 and Eq. 7:

$$\overline{K}_f = 1 + q\,(\overline{K}_t - 1) \quad \text{Eq. 6}$$

$$\acute{\sigma}_e = \frac{\sigma_e}{\overline{K}_f} \quad \text{Eq. 7}$$

in which an initial estimation of the fatigue strength of specimens with standard surface finish under alternating bending fatigue loading (σ_e) was considered as half of the ultimate tensile strength (UTS) of the base material (Table 2). The effect of dimension was neglected in the formulation of $\acute{\sigma}_e$ due to the small diameter of the specimen (6 mm as shown in Figure 5a).

2.5.2. Method 2- Local stress approach

In this approach, we adopted the local stress concept proposed by Eichlseder [39]. This method defines the stress gradient χ and relative stress gradient $\acute{\chi}$ parameters (described in Eq. 8 and Eq. 9) considering the maximum local stress (σ_{max}) to describe the stress irregularities around notches (Figure 5c):

$$\chi = \left(\frac{d\sigma}{dx}\right) \quad \text{Eq. 8}$$

$$\acute{\chi} = \left(\frac{1}{\sigma_{max}}\right)\left(\frac{d\sigma}{dx}\right) \quad \text{Eq. 9}$$

The local stress method estimates the fatigue strength of specimens with any arbitrary stress gradient, through an inter- or extrapolation of relative stress gradient in pure tensile loading (zero gradient) and that of pure bending (gradient equal to 2/b where *b* is the diameter of the specimen). Therefore, Eq. 10 can be used to estimate the fatigue strength σ_f based on the relative stress gradient $\acute{\chi}$ [39]:

$$\sigma_f = \sigma_{tf}\left(1 + \left(\frac{\sigma_{bf}}{\sigma_{tf}} - 1\right)\left(\frac{\acute{\chi}}{\left(2/b\right)}\right)^{K_D}\right) \quad \text{Eq. 10}$$

The exponent K_D describes the exponential relation between the fatigue strength and the relative stress gradient, considering the fact that an increased stress gradient decreases the rate of fatigue strength variation. The relative stress gradient was estimated using a linear elastic FE model considering a cylindrical geometry with a diameter equal to the specimen's diameter (6 mm) and with an equivalent notch embedded around the perimeter (Figure S2). This simple semi-elliptical equivalent notch geometry was defined based on the surface roughness parameters and the notch radius. In this semi-elliptical notch, the value of $\bar{\rho}$ obtained in method 1 (section 2.5.1) was used as the notch radius; notch depth was the maximum peak to valley height (S_z) and notch opening was correspondingly evaluated considering an elliptical geometry. A bending moment equivalent to the estimated fatigue strength was applied to extract the relative stress gradient $\acute{\chi}$. Then the fatigue strength was estimated using Eq. 10, considering the experimentally measured fatigue strength of the unpeened specimen (R=-1) under bending (σ_{bf}) and tension (σ_{tf}) and considering K_D equal to 0.6 based on the material characteristics. Eq. 10 considers solely the stress gradient caused by the notch; thus, for the final fatigue assessment, the effect of the notch presence on stress concentration was also implemented.

3. Results

3.1. Deformation contours and surface coverage

Figure 6a represents the indentation profile of a single impact simulation along the central path of the indent for AB and HT specimens, respectively. The dimple's diameter was estimated using Figure 6a. The magnitude of the corresponding PEEQ at the dimple's extremity was used as the threshold value for surface coverage analysis. The PEEQ threshold values were estimated to be 0.066 and 0.275 mm/mm for AB and HT specimens, respectively. Owing to the irregular surface topography, the full coverage conditions were based on the criterion that the minimum PEEQ induced in the impact area reached the threshold PEEQ value. Thus, the generation of random shots and impact sequence was continued through monitoring the evolution of nodal PEEQ within the impact area till this condition was fully satisfied on all the nodes. The final analyses indicated that the number of required shots for the full coverage was always around 200 (±10) for both AB and HT specimens. Figure 6b, represents the random distribution of the impact positions for 200 shots generated by the MATLAB code, according to the estimated dimple size. It is observed from Figure 6a that the dimple's diameter is around 10% larger while it is around 40% deeper for HT in comparison with AB, in agreement with the more ductile behavior of the former. A larger pile-up is also induced in the perimeter of the dimple in HT which suggests, along with a deeper indent, that rougher surfaces should be expected for HT series compared to the AB ones after shot peening.

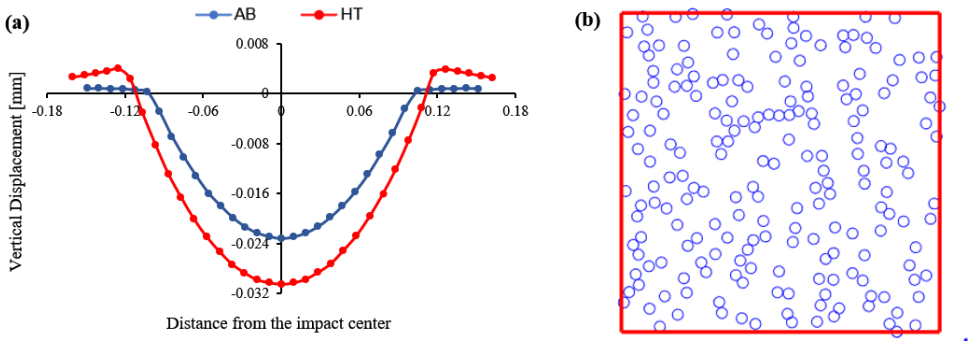

Figure 6. (a) Indentation (displacement field) profile of a single impact (b) 200 randomly generated shot positions.

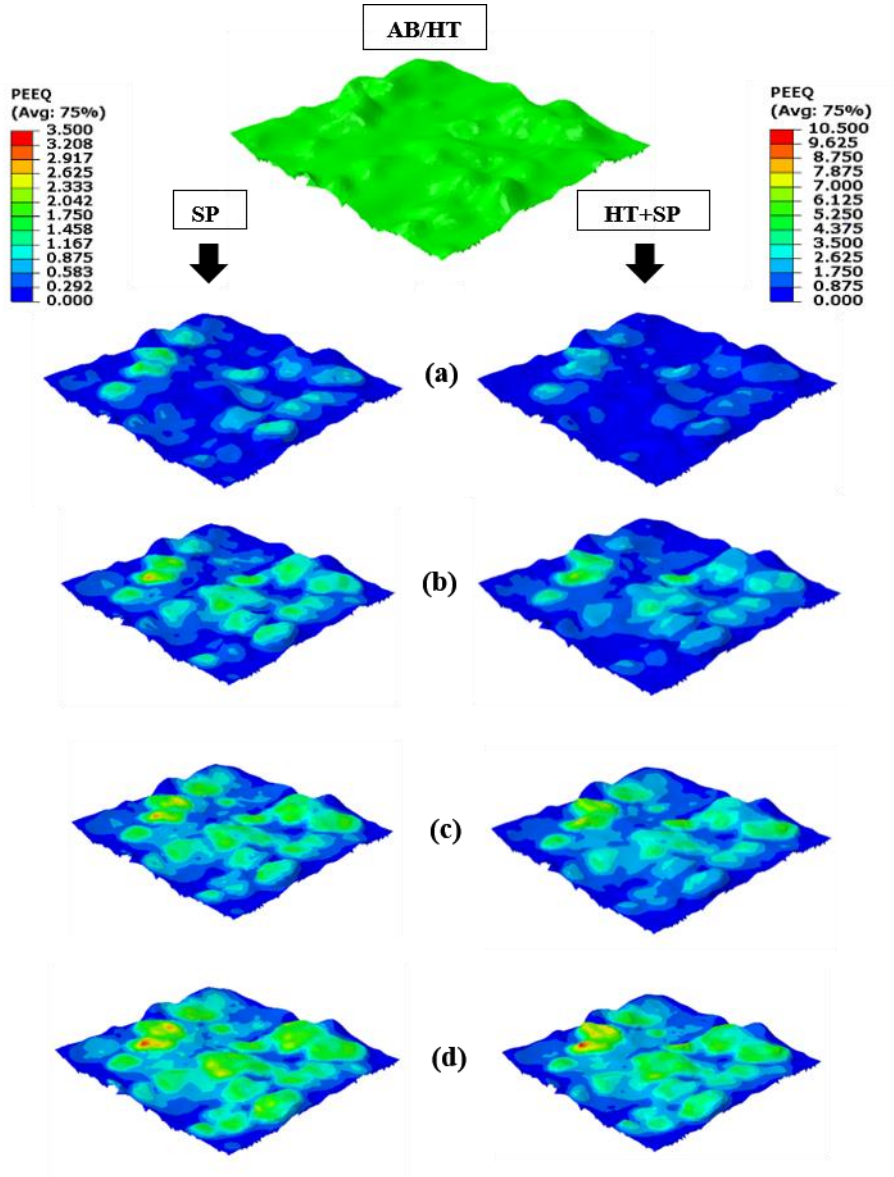

Figure 7. The evolution of the surface and equivalent plastic strain over an area of 1.2×1.2 mm^2 for SP and HT+SP specimens: (a) 50 shots, (b) 100 shots, (c) 150 shots, (d) 200 shots.

Figure 7 shows the plastic strain contours along with the evolution of surface morphology for shot peening of a representative surface at various peening intervals designated by 50, 100, 150, and 200 shots. The lower strain level at the edges is because the shot centers were only located within the impact

area (1×1 mm^2) (Figure 6b) and therefore, much lower plastic strain occurred at the borders of the represented images in Figure 7. As the number of the impacting shots increases, more plastic deformation is induced, and the morphology of the initial surface irregularities starts to change. After the application of shot peening to full coverage (Figure 7d), the maximum induced plastic strain in HT specimen is around 3 times larger than the one in AB. Considering the more ductile behavior of the HT material vs. the AB counterpart, substantially larger levels of plastic deformation were obtained in HT specimens at the identical shot peening Almen intensity.

3.2. Validation of numerical roughness analysis

To validate the developed roughness code and evaluate the effect of surface filtering (described in section 2.3.1) on the roughness data, we analyzed the .stl files experimentally obtained for scanned 1×1 mm^2 surfaces in two states of namely 'high' and 'low' resolution configurations using the developed code to extract the standard roughness parameters. High resolution refers to the original surfaces, whereas low resolution determines the transformed surfaces after filtering, as represented in Figure 2. A complete comparison of the surface roughness data is presented in Figure 8. In brief, the overall comparison of the high-resolution results obtained from the code and those experimentally obtained from the Alicona microscope indicate the validity of the developed roughness code. While the difference noted between the roughness parameters extracted from the high- and low-resolution surfaces, is more notable in the AB configuration compared to the shot peened series. A detailed comparison on the effect of surface resolution on the accuracy of the estimated roughness parameters is provided in the discussion section.

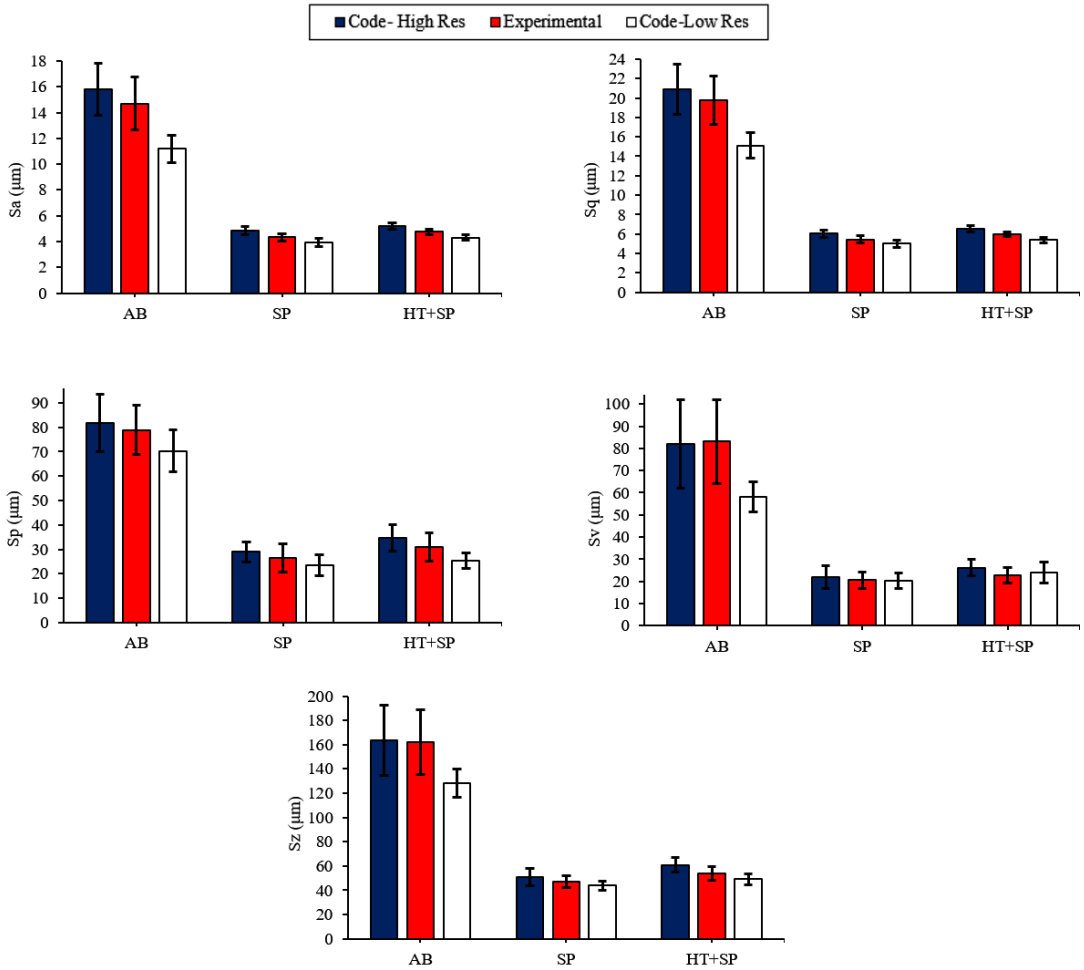

Figure 8. Areal roughness parameters of the specimens obtained experimentally compared to the ones evaluated by the developed code in high and low resolutions (all using the same stl source file).

3.3. Comparison of numerical and experimental surface roughness

To validate the developed shot peening FE model, here the surface roughness parameters obtained from the simulations are compared with the experimental data. The areal roughness parameters for all series are presented in Figure 9. Since during the filtering process, the peaks and valleys were modified, the values of S_p and S_v are not defined following their standard definitions. As an alternative, they are formulated as the average of the 5% maximum heights of the surface for S_p and the average of the 5% largest depths for S_v to account for a distribution of the actual heights and depths. Comparing the numerical and experimental data, it can be stated that most of the roughness parameters fall into the same range, considering the standard deviations (Figure 9). Larger differences are more notable for local parameters such as S_z. Although by considering the standard deviation indicated by error bars, the discrepancy of the results becomes much less significant.

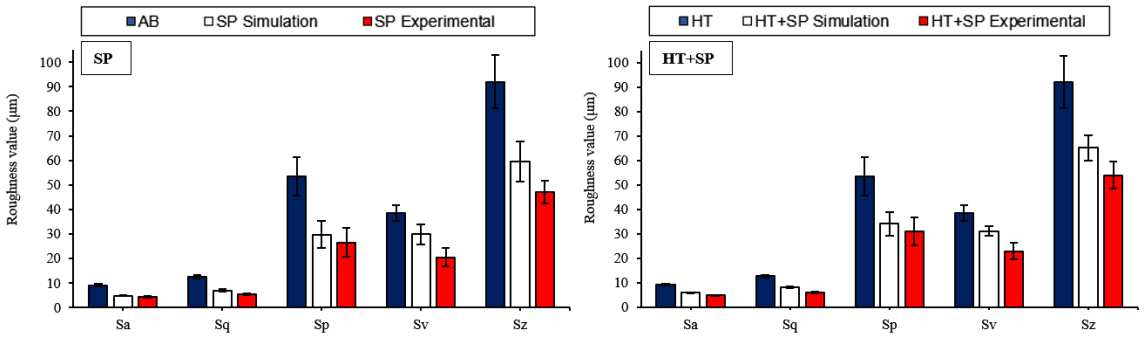

Figure 9. Comparison of the experimental and numerical surface roughness parameters.

3.4. Fatigue strength analysis

3.4.1. Fatigue estimation using equivalent notch factor

To estimate the equivalent stress concentration factor using Eq. 4, the roughness parameters S_a, S_z and S_{10z} were extracted from the numerical model. The parameter S_{10z} (Eq. 4), was defined as the sum of the average of maximum 10% heights with the average of minimum 10% depths for the SP and HT+SP surfaces obtained from simulations. Parameter m (Eq. 4) was set to 2 as the stress state is tensile-compressive under the rotating bending loading. An average $\bar{\rho}$ of all representative 1×1 mm^2 surfaces was considered to estimate the equivalent notch radii for all series. The parameters required for the calculation of $\overline{K}_t$ are reported in Table 4.

Table 4 Surface roughness parameters and equivalent valley radii for evaluation of $\overline{K}_t$

	S_a [μm]	S_z[μm]	S_{10z}[μm]	$\bar{\rho}$[μm]
SP	4.83 ± 0.2	59.7 ± 8.2	46.4 ± 7.1	73.4 ± 7.7
HT+SP	5.84 ± 0.1	65.1 ± 5.3	49.9 ± 5.5	57 ± 5.3

The parameters calculated using Eq. 4 to Eq. 7 and the estimated fatigue strength data together with the experimental fatigue strengths are reported in Table 5. The last column in Table 5 depicts the error percentage between the experimental and estimated fatigue strengths.

Table 5 Parameters required for equivalent notch factor method and comparison of estimated fatigue strength with the experimental fatigue test data

	$\overline{K}_t$	q	$\overline{K}_f$	Estimated fatigue strength (MPa)	Experimental fatigue strength (MPa) [13]	Error (%)
SP	1.17	0.98	1.17	168	185 ± 13	9.0
HT+SP	1.27	0.92	1.25	106	102 ± 4	4.3

3.4.2. Fatigue estimation using local stress approach

The parameters necessary for implementing Eq. 9 and Eq. 10 and comparing the estimated and the experimental fatigue strength data are listed in

Table 6 for SP and HT+SP specimens. The fatigue strengths in bending and tension were considered as 0.5 and 0.4 times the UTS of the base material, respectively [40, 41]. The diameter of the hourglass specimen, b, was set as the minimum diameter of the fatigue test specimen (Figure 5a). Constant K_D was determined based on the proposed value by Eichlseder for a similar alloy, i.e. AlSi7Mg [42]. Moreover, K_t parameter was derived directly using the ratio of the local maximum stress at the root of the equivalent notch obtained from the FE model and the applied nominal bending stress (σ_{bf}). The obtained results were found to be closer to the experimental data compared to those obtained by equivalent notch factor.

Table 6 Parameters required for local stress method and comparison of estimated fatigue strength with the experimental fatigue test data

	σ_{bf} (MPa)	σ_{tf} (MPa)	K_t	$\acute{\chi}$ (1/mm)	Estimated fatigue strength (MPa)	Experimental fatigue strength (MPa) [13]	Error (%)
SP	196.5	157.2	2.65	9.81	172	185 ± 13	6.8
HT+SP	132.5	106	2.69	7.98	105	102 ± 4	3.5

4. Discussion

A detailed numerical model was developed to simulate the application of the shot peening process on the irregular as-built surface of LPBF AlSi10Mg specimens. The surface morphology obtained from the simulations was then post-processed to extract the standard profile and surface roughness parameters and then correlate them to the fatigue strength of the specimens using analytical approaches. According to the simulation results in Figure 7a and b for both AB and HT surfaces, the induced deformations are mostly concentrated in peaked areas. This is because the starting shots impacted mostly the high peak regions, and the areas between them (valley regions) were contacted much less with the impacting shots due to the rough nature of the initial AB surface. As the shot number increased, the peaks were smoothened more effectively under the induced deformations by the impacts, and consequently, the deformations started to spread into valley areas (Figure 7c and d). At full coverage level for both AB and HT specimens, a pronounced non-uniform plastic deformation contour is observed on the surfaces. The numerical simulation results, in line with the experimental data, indicated a decrease in the roughness parameters after the application of the shot peening process. This, in turn, reveals that the initial irregular morphology of the AB/HT surfaces has been smoothened upon peening, evolving into a more regular surface with reduced surface roughness. The more common case is to start from an initially smooth surface and after shot peening treatment with full coverage, the final morphology evolves to a higher surface roughness [43, 44]. However, when the initial surface is very irregular with large roughness parameters, as in the case of LPBF material, the shot peening treatment acts differently, and consequently, the roughness is reduced by the application of full coverage shot peening.

A MATLAB code was developed for quantitative analysis of the surface features obtained from the shot peening simulation. The validity and accuracy of the developed code were confirmed by comparing the calculated roughness parameters using the code (for high-resolution surfaces) with those directly obtained from the microscope (Figure 8). The small discrepancy could be due to the difference in the selected scanned areas in the experiment compared to the ones processed by the code.

On the other hand, regarding the effect of surface transformation that was implemented to reduce the computational costs, a comparison was made between high resolution and low-resolution surfaces. The low-resolution data showed a notable difference with the high resolution (and thus the experimental) parameters for the AB specimen; for instance, deviations of around 23% were detected for S_a and S_q parameters. While, interestingly, for the SP and HT+SP series, the differences between the roughness parameters of the low-resolution surfaces and the high resolution/experimental data were much less significant; for example, for S_a and S_q of the SP and HT+SP specimens, the differences between the average values of corresponding low- and high-resolution analyses were found to be less than 9%. Considering the data scatter (standard deviations), it can be noted that the values extracted from low- and high-resolution surfaces for the shot peened series fall even into the same ranges. We postulate that the lower sensitivity of shot peened surfaces to the initial surface definition is mainly attributed to the

higher regularity of the shot peened surfaces compared to the AB ones. In AB configurations the presence of multiple local sharp peaks and deep valleys makes the effect of the surface resolution more evident. These analyses indicate that despite the discrepancies in the case of the AB series, exploiting the low-resolution data (for the sake of computational costs) is a valid strategy for assessing the surface roughness after SP treatment.

Higher experimental roughness parameters are detected for HT+SP specimens compared to the SP series (Figure 8). The same observation can also be noticed from the simulation results (Figure 9). Therefore, the developed FE model is able to correctly predict the surface roughness relation between these two series, by implementing the corresponding elastoplastic behavior of the base material in AB and HT configurations. The higher ductility induced after heat treatment led to higher roughness parameters for HT+SP induced by higher extents of deformation and easier generation of pile-ups.

Figure 9 also demonstrated that for SP and HT+SP specimens, most estimated roughness parameters fall into the same range as the experimental data. By considering the standard deviation indicated by error bars, the discrepancy of the few diverging parameters becomes less significant. In addition, the randomness of the irregular initial AM surface as well as the intrinsic random nature of shot peening impacts in terms of sequence and position could potentially be additional sources of data uncertainty.

The mismatch observed between some parameters could be attributed to various sources including the limitations induced by the intrinsic randomness of the shot peening treatment and the small surface area considered in the modeling due to computational costs. By enlarging the representative surface areas, a more accurate surface texture assessment could be expected. Overall, the results indicate that the developed shot peening model is able to successfully evaluate the final surface topography at full coverage.

The surface roughness data extracted from the simulations were used for fatigue life estimation using simple analytical approaches by accounting for the stress concentration caused by surface irregularities. The equivalent notch approach is based on a method implemented for fatigue strength estimation of AM materials in AB configurations by Pegues et al. [9]. They considered an equivalent notch using the roughness parameters and effective notch radius to estimate the notch sensitivity factor q and equivalent fatigue notch factor $\overline{K}_f$. By having the fatigue strength of an unnotched specimen, the fatigue strength for the rough AM surfaces could be obtained. In the second method, considering a semi-elliptical notch defined by roughness parameters and notch radius, the relative stress gradient of the specimens under bending was calculated implementing a linear elastic FE model. Afterwards, by means of an inter- or extrapolation of relative stress gradient in pure tension and pure bending, the fatigue strengths were estimated [45].

As reported in Table 5, the stress concentration factor of the more irregular specimen, i.e., HT+SP, is higher than that of SP. This illustrates that the proposed approach for fatigue analysis using surface roughness parameters correctly captures the trend of $\overline{K}_t$ and $\overline{K}_f$. Additionally, a larger notch radius is expected to lead to a lower stress gradient and therefore, a higher notch sensitivity [46]. This is perfectly predicted in the case under study since the calculated notch sensitivity factor q of the rougher HT+SP specimen was lower than that of SP. This trend confirms the suitability of the proposed definition for the effective valley radii $\bar{\rho}$.

The data presented in Table 5 and Table 6 also indicate that both analytical methods implemented for calculation of fatigue strength using the surface roughness parameters can effectively provide comparable estimations with the experimental data showing in all cases an error lower than 10%. The proposed analytical approaches do not take residual stresses and surface hardening due to shot peening into account, which may have an influence on the fatigue behavior. However, the good accordance of the estimated fatigue strengths with the experimental data suggests a limited effect of the latter two factors in the processed specimens of the current study. During the cyclic loading in the case of SP and HT+SP specimens, the compressive residual stresses might have been partially relaxed. This was proven by X-ray diffraction (XRD) measurement of residual stresses on a specimen before and after fatigue test subjected to the same alternate stresses as the corresponding fatigue strength for 3 million cycles (see Figure S3). The measurements show that, with the considered shot peening parameters, the residual stresses are quite below the yield stress of the materials, thus they have a reduced effectiveness in retarding fatigue crack propagation (this is the main effect attributed to the shot peening residual stresses). Also, regarding the effects of shot peening on microstructure, the authors' previous study

indicated that the parameters used for shot peening do not lead to significant alteration of the top surface layer microstructure in AlSi10Mg specimens [13]. Thus, in this case, the main contribution of shot peening was found to be the notch effect reduction related to the surface roughness rather than notably altering the crack propagation rate. Therefore, it can be claimed that implementing the roughness parameters and average valley radii of the obtained shot peened surfaces from the developed numerical FE model in the proposed fatigue analysis methodologies can lead to an accurate estimation of fatigue strength for these specimens, despite disregarding the effect of residual stresses. To sum up, it was substantiated that both geometry-based and local stress methods can estimate the fatigue strength of the studied specimens with reasonably good accuracies. In order to expand the model limits to other materials or processing parameters, the model should be further upgraded to consider the effects of residual stresses, surface hardening and potential microstructural alteration based on the applied shot peening parameters.
One limitation of the developed approach could be the potential presence of surface open defects, which are not traceable using optical microscopy; this aspect may make the procedure dependent on the depth and geometrical complexity of the surface defects. In the cases, where deep and inclined defects exist, the process could be improved using other techniques such as micro-CT to replace optical microscopy and guarantee a high degree of accuracy in surface state estimation before and after the shot peening treatment. Another aspect that could be improved is to vary the impact angle of the shots as a function of target geometry in the developed model. This approach that is indeed used in practical robotized shot peening treatment, can be very useful especially in the case of complex target geometries.

5. Conclusion

In this study, a hybrid numerical-analytical framework was proposed to estimate the effect of shot peening treatment on the fatigue strength of AlSi10Mg alloy fabricated using laser powder bed fusion (LPBF). Four series of specimens in the as-built (AB), heat-treated (HT), shot peened (SP), and heat-treated and shot peened (HT+SP) conditions were considered. A numerical finite element (FE) model of the shot peening process was developed to simulate the effect of the peening process on the surface topography of the irregular AB and HT surfaces. A MATLAB code was developed to post-process the output of the simulations and extract the areal surface roughness parameters. Two analytical methodologies based on the geometry and local stress concepts were integrated to estimate the fatigue strength after shot peening. Considering the obtained results, the following conclusions can be drawn:

- The developed shot peening model and the post-processing code were successfully validated in comparison with experimental roughness data. Areal roughness parameters of the shot peened specimens extracted from the developed numerical model demonstrated good accordance with those of the experiments. The results fall into the same ranges considering the scatter of data, which can be justified by the randomness of the initial surface features in AM specimens as well as the intrinsic randomness of impact sequence and position in shot peening.
- Reduction of surface roughness parameters after shot peening confirmed the role of this impact-based surface treatment in substantially smoothening the high local irregularities of the AB surfaces inducing a more regular surface morphology. The application of shot peening resulted in an overall reduction of 40-50% in areal roughness parameters for the AB specimens. However, when applied to the more ductile HT surfaces, an overall reduction of around 30-37% was achieved. This difference is due to the high kinetic energy of the multiple impacts that resulted in the easier generation of pile-ups in the more ductile HT series.
- A satisfactory estimation of fatigue strength was obtained with an estimation error of less than 10% using the developed hybrid numerical-analytical framework. This indicates that the proposed framework provides a consistent and reliable procedure to envisage the fatigue performance of materials manufactured by LPBF after shot peening. Seemingly, both analytical methods show comparable accuracy. Nevertheless, the first method is more convenient as it does not require the development of an extra FE model for the calculation of the stress gradient.
- Although the implemented analytical fatigue analyses do not consider the shot peening residual stresses, a satisfactory approximation of fatigue strength was demonstrated. This could be justified by a partial relaxation of residual stresses in the SP and HT+SP AlSi10Mg specimens, promoted also by the presence of internal pores; an initial conservative choice of the shot peening parameters led to low

residual stresses, the partially relaxation of which with the load cycle application was not enough to positively affect the final fatigue strength. This suggest that the optimization of shot peening treatment and the possibility to consider higher treatment intensity.

Overall, the developed hybrid methodology for estimating the effect of shot peening on the irregular surface morphology of LPBF material combined with analytical approaches show a high potential to be used for assessing the effect of shot peening on homogenization of the as-built surfaces and can evaluate their contribution to fatigue strength enhancement. This package can be significantly practical for designing the shot peening process and parameter optimization in AM sector, as it can substantially reduce if not eliminate the needed costly experimental tuning of the shot peening parameters and fatigue tests. Future steps will be to account for the possible effective residual stresses induced by more intense treatments in the analytical calculations.

Supplementary data

Table S1 Definition of the roughness parameters based on ISO 4287:1997 and ISO 25178

Arithmetic average height	$R_a = \frac{1}{l}\int_0^l \lvert z(x)\rvert \, dx$
Root mean square deviation	$R_q = \sqrt{\frac{1}{l}\int_0^l \{z(x)\}^2 \, dx}$
Maximum valley to peak height	$R_t = R_p + R_v$
Ten-points height	$R_z = \frac{1}{5}\left(\sum_{i=1}^{5} p_i - \sum_{i=1}^{5} v_i\right)$
Areal arithmetic average height	$S_a = \frac{1}{M.N}\sum_{j=1}^{N}\sum_{i=1}^{M} \lvert z(x_i, y_j)\rvert$
Areal root mean square deviation	$S_q = \sqrt{\frac{1}{M.N}\sum_{j=1}^{N}\sum_{i=1}^{M} \lvert z^2(x_i, y_j)\rvert}$
Areal maximum valley to peak height	$S_z = \lvert S_p + S_v\rvert$
Areal ten-points height	$S_{10z} = \frac{\sum_{i=1}^{5} p_i + \sum_{i=1}^{5} v_i}{5}$

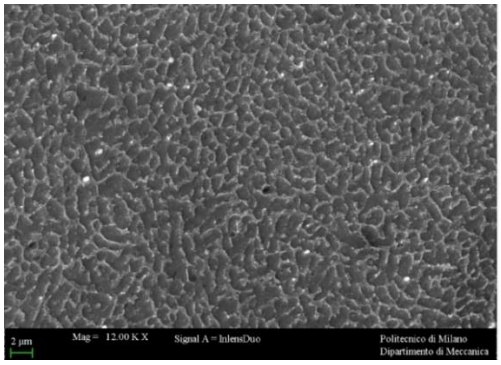

Figure S1. Scanning electron micrograph of AB specimen's lateral cross section after etching for 20 s using Keller's reagent (95% pure H2O, 1% HF, 1.5% HCl, 2.5% HNO3).

FE model for local stress approach:

The cylinder used for FE model is shown in Figure S2a, whereas the equivalent notch located at the middle of the cylinder length around its perimeter is illustrated in Figure S2b. A bending moment was applied in z direction with a magnitude evaluated from the fatigue strength of material in bending estimated as half its ultimate tensile strength.

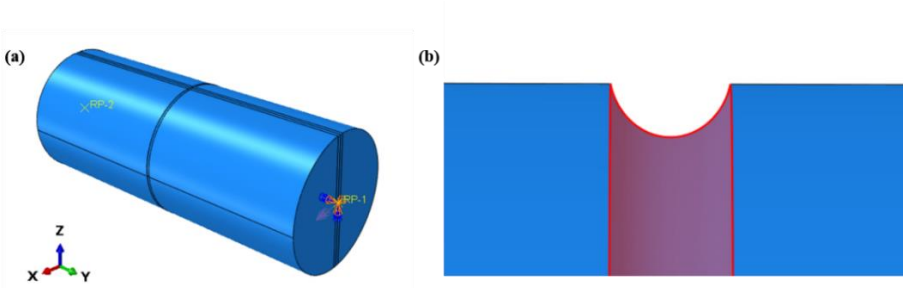

Figure S2. Geometry of the model used for obtaining stress gradient: a) isometric view and b) close-up of the defined equivalent notch

Residual stress measurement:

The distribution of the residual stresses was measured using X-ray diffraction (XRD) method. The measurement was done along a path perpendicular to the build direction using AST X-Stress 3000 portable X-ray diffractometer with Cr CrKα radiation, at a diffraction angle (2θ) of 139° corresponding to 311-reflex scanned with a total of 7 tilts in the range of −45° to 45° along three rotations of 0°, 45° and 90° with a step size of 0.028° based on the sin2(ψ) method. For in-depth measurements, electropolishing was used to remove the material layer-by-layer on a circular area with a radius of 0.25 cm in a solution of 94% CH_3COOH, 6% $HClO_4$ at a voltage of 35 V. Depth measurements were done using a precision Mitutoyo micrometer (IDCH0530/05060).

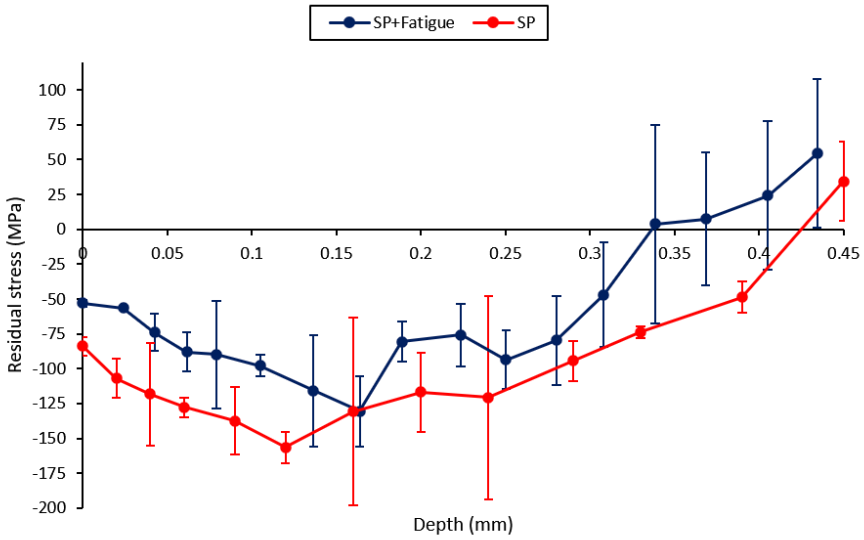

Figure S3. Comparison of residual stresses of SP specimen before and after fatigue tests (tested under the corresponding fatigue strength up to 3 million cycles).

Data Availability Statement

The raw/processed data required to reproduce these findings can be shared upon request.

Bibliography

1. Tarantino, M.G., O. Zerhouni, and K. Danas, *Random 3D-printed isotropic composites with high volume fraction of pore-like polydisperse inclusions and near-optimal elastic stiffness.* Acta Materialia, 2019. **175**: p. 331-340.
2. Zerhouni, O., M.G. Tarantino, and K. Danas, *Numerically-aided 3D printed random isotropic porous materials approaching the Hashin-Shtrikman bounds.* Composites Part B: Engineering, 2019. **156**: p. 344-354.
3. Thomas, D.S. and S.W. Gilbert, *Costs and cost effectiveness of additive manufacturing.* NIST special publication, 2014. **1176**: p. 12.
4. Mower, T.M. and M.J. Long, *Mechanical behavior of additive manufactured, powder-bed laser-fused materials.* Materials Science and Engineering: A, 2016. **651**: p. 198-213.
5. Beretta, S., M. Gargourimotlagh, S. Foletti, A. du Plessis, and M. Riccio, *Fatigue strength assessment of "as built" AlSi10Mg manufactured by SLM with different build orientations.* International Journal of Fatigue, 2020. **139**: p. 105737.
6. Vayssette, B., N. Saintier, C. Brugger, M. El May, and E. Pessard, *Numerical modelling of surface roughness effect on the fatigue behavior of Ti-6Al-4V obtained by additive manufacturing.* International Journal of Fatigue, 2019. **123**: p. 180-195.
7. Sanaei, N. and A. Fatemi, *Analysis of the effect of surface roughness on fatigue performance of powder bed fusion additive manufactured metals.* Theoretical and Applied Fracture Mechanics, 2020. **108**: p. 102638.
8. Chen, Z., S. Cao, X. Wu, and C.H.J. Davies, *13 - Surface roughness and fatigue properties of selective laser melted Ti–6Al–4V alloy*, in *Additive Manufacturing for the Aerospace Industry*, F. Froes and R. Boyer, Editors. 2019, Elsevier. p. 283-299.
9. Pegues, J., N. Shamsaei, M. Roach, and R. Williamson, *Fatigue life estimation of additive manufactured parts in the as-built surface condition.* Material Design & Processing Communications, 2019. **1**: p. e36.
10. Arola, D. and M. Ramulu, *An Examination of the Effects from Surface Texture on the Strength of Fiber Reinforced Plastics.* Journal of Composite Materials - J COMPOS MATER, 1999. **33**: p. 102-123.
11. Maleki, E., S. Bagherifard, M. Bandini, and M. Guagliano, *Surface post-treatments for metal additive manufacturing: Progress, challenges, and opportunities.* Additive Manufacturing, 2021. **37**: p. 101619.

12. Bagherifard, S., *Enhancing the Structural Performance of Lightweight Metals by Shot Peening.* Advanced Engineering Materials, 2019. **21**(7): p. 1801140.
13. Bagherifard, S., N. Beretta, S. Monti, M. Riccio, M. Bandini, and M. Guagliano, *On the fatigue strength enhancement of additive manufactured AlSi10Mg parts by mechanical and thermal post-processing.* Materials & Design, 2018. **145**: p. 28-41.
14. Maamoun, A., M. Elbestawi, and S.C. Veldhuis, *Influence of Shot Peening on AlSi10Mg Parts Fabricated by Additive Manufacturing.* Journal of Manufacturing and Materials Processing, 2018. **2**: p. 40.
15. Kahlin, M., H. Ansell, D. Basu, A. Kerwin, L. Newton, B. Smith, and J.J. Moverare, *Improved fatigue strength of additively manufactured Ti6Al4V by surface post processing.* International Journal of Fatigue, 2020. **134**: p. 105497.
16. Wycisk, E., C. Emmelmann, S. Siddique, and F. Walther, *High Cycle Fatigue (HCF) Performance of Ti-6Al-4V Alloy Processed by Selective Laser Melting.* Advanced Materials Research, 2013. **816-817**: p. 134-139.
17. Pintado, C., J. Vázquez Valeo, J. Domínguez, A. Periñán, M. García, F. Lasagni, S. Bernarding, S. Slawik, F. Mücklich, F. Boby, and L. Hackel, *Effect of surface treatment on the fatigue strength of additive manufactured Ti6Al4V alloy.* Frattura ed Integrità Strutturale, 2020. **14**: p. 337-344.
18. Soyama, H. and F. Takeo, *Effect of Various Peening Methods on the Fatigue Properties of Titanium Alloy Ti6Al4V Manufactured by Direct Metal Laser Sintering and Electron Beam Melting.* Materials, 2020. **13**: p. 2216.
19. Benedetti, M., E. Torresani, M. Leoni, V. Fontanari, M. Bandini, C. Pederzolli, and C. Potrich, *The effect of post-sintering treatments on the fatigue and biological behavior of Ti-6Al-4V ELI parts made by selective laser melting.* Journal of the Mechanical Behavior of Biomedical Materials, 2017. **71**: p. 295-306.
20. Aboulkhair, N.T., I. Maskery, C. Tuck, I. Ashcroft, and N.M. Everitt, *The microstructure and mechanical properties of selectively laser melted AlSi10Mg: The effect of a conventional T6-like heat treatment.* Materials Science and Engineering: A, 2016. **667**: p. 139-146.
21. Gharavi, F., K.A. Matori, R. Yunus, and N.K. Othman, *Corrosion behavior of friction stir welded lap joints of AA6061-T6 aluminum alloy.* Materials Research, 2014. **17**(3): p. 672-681.
22. Bagherifard, S., R. Ghelichi, and M. Guagliano, *A numerical model of severe shot peening (SSP) to predict the generation of a nanostructured surface layer of material.* Surface and Coatings Technology, 2010. **204**(24): p. 4081-4090.
23. Kim, T., J.H. Lee, H. Lee, and S.-k. Cheong, *An area-average approach to peening residual stress under multi-impacts using a three-dimensional symmetry-cell finite element model with plastic shots.* Materials & Design, 2010. **31**(1): p. 50-59.
24. Guagliano, M., *Relating Almen intensity to residual stresses induced by shot peening: a numerical approach.* Journal of Materials Processing Technology, 2001. **110**(3): p. 277-286.
25. Ludwik, P., *Elemente der Technologischen Mechanik*. 1909: Springer Berlin Heidelberg.
26. Wu, J., H. Liu, P. Wei, C. Zhu, and Q. Lin, *Effect of shot peening coverage on hardness, residual stress and surface morphology of carburized rollers.* Surface and Coatings Technology, 2020. **384**: p. 125273.
27. Lin, Q., H. Liu, C. Zhu, D. Chen, and S. Zhou, *Effects of different shot peening parameters on residual stress, surface roughness and cell size.* Surface and Coatings Technology, 2020. **398**: p. 126054.
28. Wu, J., H. Liu, P. Wei, Q. Lin, and S. Zhou, *Effect of shot peening coverage on residual stress and surface roughness of 18CrNiMo7-6 steel.* International Journal of Mechanical Sciences, 2020. **183**: p. 105785.
29. Miao, H.Y., S. Larose, C. Perron, and M. Lévesque, *On the potential applications of a 3D random finite element model for the simulation of shot peening.* Advances in Engineering Software, 2009. **40**(10): p. 1023-1038.
30. Gadelmawla, E.S., M.M. Koura, T.M.A. Maksoud, I.M. Elewa, and H.H. Soliman, *Roughness parameters.* Journal of Materials Processing Technology, 2002. **123**(1): p. 133-145.
31. Dixon, W.J. and F.J. Massey Jr, *Introduction to statistical analysis*. Introduction to statistical analysis. 1951, New York, NY, US: McGraw-Hill. x, 370-x, 370.

32. Arola, D. and C. Williams, *Estimating the fatigue stress concentration factor of machined surfaces.* International Journal of Fatigue, 2002. **24**: p. 923-930.
33. McKelvey, S.A. and A. Fatemi, *Surface finish effect on fatigue behavior of forged steel.* International Journal of Fatigue, 2012. **36**(1): p. 130-145.
34. Greenwood, J.A. and K.L. Johnson, *A unified theory of surface roughness.* Proceedings of the Royal Society of London. A. Mathematical and Physical Sciences, 1984. **393**(1804): p. 133-157.
35. Poon, C.Y. and B. Bhushan, *Surface roughness analysis of glass-ceramic substrates and finished magnetic disks, and Ni-P coated Al-Mg and glass substrates.* Wear, 1995. **190**(1): p. 89-109.
36. Dowling, N.E., *Mechanical behavior of materials : engineering methods for deformation, fracture, and fatigue*. 1993: Englewood Cliffs, N.J. : Prentice Hall, [1993] ©1993.
37. Karry, R.W., T.J. Dolan, and S. Illinois Univ At Urbana Engineering Experiment, *INFLUENCE OF GRAIN SIZE ON FATIGUE NOTCH-SENSITIVITY*. 1953, Ft. Belvoir: Defense Technical Information Center.
38. Maamoun, A.H., M. Elbestawi, G.K. Dosbaeva, and S.C. Veldhuis, *Thermal post-processing of AlSi10Mg parts produced by Selective Laser Melting using recycled powder.* Additive Manufacturing, 2018. **21**: p. 234-247.
39. Eichlseder, W., *Fatigue analysis by local stress concept based on finite element results.* Computers & Structures, 2002. **80**(27): p. 2109-2113.
40. *Fatigue of metals. P. G. Forrest. Oxford 1962, Pergamon Press Ltd., 425 S., 154 Abb., 84 Tab., Preis sh 70.–.* Materials and Corrosion, 1963. **14**(7): p. 630-630.
41. Tóth, L. and S.Y. Yarema, *Formation of the science of fatigue of metals. Part 1. 1825–1870.* Materials Science, 2006. **42**(5): p. 673-680.
42. Eichlseder, W., *Lebensdauervorhersage auf Basis von Finite Elemente Ergebnissen.* Materialwissenschaft und Werkstofftechnik, 2003. **34**(9): p. 843-849.
43. Bagherifard, S., R. Ghelichi, and M. Guagliano, *Numerical and experimental analysis of surface roughness generated by shot peening.* Applied Surface Science, 2012. **258**(18): p. 6831-6840.
44. Tu, F., D. Delbergue, T. Klotz, A. Bag, H. Miao, C. Bianchetti, M. Brochu, P. Bocher, and M. Levesque, *Discrete element-periodic cell coupling model and investigations on shot stream expansion, Almen intensities and target materials.* International Journal of Mechanical Sciences, 2018. **145**: p. 353-366.
45. Bagherifard, S. and M. Guagliano, *Application of different fatigue strength criteria on shot peened notched parts. Part 2: nominal and local stress approaches.* Applied Surface Science, 2014. **289**: p. 173-179.
46. Pogačnik, A. and M. Kalin, *How to determine the number of asperity peaks, their radii and their heights for engineering surfaces: A critical appraisal.* Wear, 2013. **300**: p. 143-154.